# Crystallization kinetics and thermodynamics of an Ag-In-Sb-Te phase change material using complementary *in situ* microscopic techniques

Isak McGieson,<sup>1</sup> Victoriea L. Bird,<sup>2</sup> Christopher M. Barr,<sup>3</sup> Khalid Hattar,<sup>3</sup> Bryan W. Reed,<sup>4</sup> Joseph T. McKeown,<sup>5</sup> Feng Yi,<sup>6,a</sup> David A. LaVan,<sup>6,b</sup> and M. K. Santala<sup>2,c</sup>

#### **Abstract**

The crystallization of an amorphous Ag-In-Sb-Te (AIST) phase change material (PCM) is studied using multiple *in-situ* imaging techniques to directly quantify crystal growth rates over a broad range of temperatures. The measurable growth rates span from  $\approx 10^{-9}$  m/s to  $\approx 20$  m/s. Recent results using dynamic transmission electron microscopy (TEM), a photo-emission TEM technique, and TEM with sub-framed imaging are reported here and placed into the context of previous growth rate measurements on AIST. Dynamic TEM experiments show a maximum observed crystal growth rate for as-deposited films to be > 20 m/s. It is shown that crystal growth above the glass transition can be imaged in a TEM through use of sub-framing and a high-frame-rate direct electron detection camera. Challenges associated with the determination of temperature during *in situ* TEM experiments are described. Preliminary nanocalorimetry results demonstrate the feasibility of collecting thermodynamic data for crystallization of PCMs with simultaneous TEM imaging.

**Keywords**: calorimetry; crystallization; phase transformations; transmission electron microscopy (TEM); Ag-In-Sb-Te

<sup>&</sup>lt;sup>1</sup> Department of Physics, Oregon State University, Corvallis, OR, USA

<sup>&</sup>lt;sup>2</sup> School of Mechanical, Industrial, and Manufacturing Engineering, Oregon State University, Corvallis, OR, USA

<sup>&</sup>lt;sup>3</sup> Center for Integrated Nanotechnologies, Sandia National Laboratories, Albuquerque, NM, USA

<sup>&</sup>lt;sup>4</sup> Integrated Dynamic Electron Solutions, Inc., Pleasanton, CA, USA

<sup>&</sup>lt;sup>5</sup> Materials Science Division, Lawrence Livermore National Laboratory, Livermore, CA, USA

<sup>&</sup>lt;sup>6</sup> Materials Measurement Science Division, Material Measurement Laboratory, National Institute of Standards and Technology, Gaithersburg, MD, USA

a ORCID 0000-0002-8269-3685

<sup>&</sup>lt;sup>b</sup> ORCID 0000-0002-1952-0028

<sup>&</sup>lt;sup>c</sup> Author to whom correspondence should be addressed. E-mail: melissa.santala@oregonstate.edu

## 1. Introduction

Phase change materials (PCMs) are semi-conducting alloys with distinct optical and electrical properties in the amorphous (glassy) and crystalline phases that make them useful for memory applications. PCMs were first produced in the 1960s<sup>1</sup> and developed for optical media (compact discs) in the 1980s.<sup>2</sup> More recently PCMs have been incorporated into PCM-based random-access memory (PRAM) and may be used in memristor-based memory<sup>3</sup> and neuromorphic computing,<sup>4</sup> though competitive switching speeds and reliability still pose challenges to be overcome.<sup>5</sup> In PCMbased memory devices, amorphous bits are written in a crystalline PCM layer melt-quenching with laser or Joule heating. Quenching a PCM into a glass is possible, but requires cooling rates of  $\approx 10^{10}$  K/s.<sup>6,7</sup> In re-writable media the amorphous bits are erased by re-crystallization also induced with the laser or Joule heating. It must be possible to crystallize an amorphous bit in nanoseconds, or less than a nanosecond if the materials are to be competitive for dynamic random-access memory.<sup>8</sup> The crystallization of the amorphous phase is necessarily slower than the melt-quench process (otherwise the amorphous phase could not be formed by melt-quenching) and is therefore the data-rate-limiting process. The amorphous phase must also be stable against crystallization for long-term data retention at device operating temperatures. Thus, the crystallization kinetics of PCMs over a range of temperatures from room temperature, T<sub>RT</sub>, up to the melting temperature, T<sub>m</sub>, are important for the function of PCM-based memory devices. There are few materials that satisfy the memory requirements of high contrast in opto-electronic properties between the amorphous and crystalline phases, speed of crystallization, and amorphous stability, so the crystallization kinetics are not only of practical technological importance but are also important to understanding the limits of glass-forming behavior. Crystal growth rates relevant to memory devices span orders of magnitude and fundamental questions regarding PCM crystallization mechanisms remain open, partly due to the difficulty in measuring crystallization kinetics in certain temperature regimes.

Crystallization kinetics and liquid fragility, m, are generally viewed as key to understanding glass stability across all classes of glass-forming materials, which include strong glass formers such as silica-based materials traditionally used in glass making, as well as relatively poor glass formers such as PCMs and metallic glasses. The challenge in describing the crystallization kinetics of PCMs lies in the difficulty in measuring thermodynamic and kinetic parameters from the glass transition temperature,  $T_g$ , to the melting temperature,  $T_m$ , particularly at intermediate

temperatures where the maximal growth rate,  $u_{max}$ , occurs. The crystal growth rate, u, has been directly measured for a broad range of temperatures from  $T_g$  to  $T_m$ , for a number of good glass formers owing to their low crystal growth rates, u, over the whole temperature range and with  $u_{max} < 10^{-6}$  m/s. In contrast,  $u_{max}$  in PCMs can exceed 10 m/s. In the range between  $T_g$  and the temperature where  $u_{max}$  is reached, it is extremely challenging to measure u through microscopic methods, because the limited time available between nucleation and the completion of crystallization and the small size of the crystalline grains demands both high spatial and temporal resolution. This has led to the application of indirect methods to study crystallization in PCMs such as differential scanning calorimetry (DSC)<sup>11-14</sup> or reflectivity<sup>12, 15</sup> in order to find the temperature dependence of u, the results of which do not always fit neatly into existing models of glass behavior.

Direct microscopic methods of measuring crystal growth have emerged in recent years, which could help more completely characterize crystallization behavior. The microscopic methods that have been, or can be, applied to PCMs are mapped to a schematic plot of u(T) from below  $T_g$  up to T<sub>m</sub> in FIG. 1(a). This is for a generalized PCM, so the position of T<sub>g</sub> relative to the experimentally accessible range is approximate. Ex situ atomic force microscopy (AFM)<sup>16</sup> and in situ optical microscopy<sup>17</sup> are suited for the low temperature, low u regime. The use of a high-speed camera<sup>18</sup> can extend the range of optical microscopy to almost the mm/s range, but optical microscopy is still limited by the spatial resolution, especially for PCMs with high nucleation rates which lead to sub-micron grains. In situ TEM offers higher spatial resolution and, when combined with high-speed direct electron detection cameras, extends the range of what is experimentally accessible beyond AFM and optical microscopy. The development of the nanosecond-resolution photo-emission technique, dynamic TEM (DTEM), has enabled imaging crystal growth around  $u_{max}^{10, 19}$  and the recent introduction of sub-framing and compressive sensing, which can effectively increase the frame rate of any TEM camera, 20 can be used to fill the gap between "conventional" in situ TEM and DTEM. When coupled with simultaneous nanocalorimetry these techniques may help resolve outstanding questions regarding the crystallization behavior of undercooled PCM liquids.

In this work, in situ TEM imaging techniques with high temporal resolution are used to directly quantify  $u_{max}$  in an Ag-In-Sb-Te (AIST) PCM alloy with a nominal composition of Ag<sub>3</sub>In<sub>4</sub>Sb<sub>76</sub>Te<sub>17</sub> and to demonstrate the path for directly measuring u(T) in the important range above T<sub>g</sub>. DTEM

is used to find  $u_{max}$  and estimate the maximum nucleation rate. These new data are placed in context of other measurements of u in AIST and are used to constrain a model of crystal growth in undercooled liquid. It is also shown that crystal growth above  $T_g$  can be imaged during in situ TEM using sub-framing and a high-frame-rate direct electron detection camera. Preliminary nanocalorimetry results are presented using a platform that will allow simultaneous TEM observations. This will enable seamless integration of thermodynamic and kinetic measurements in the undercooled liquid near  $T_g$ .

## 2. Background

### 2.1 Ag-In-doped Sb-Te PCMs

Ag-In-doped Sb-Te (AIST) alloys are an important group of PCMs that have been used in rewriteable optical discs<sup>21</sup> and in digital versatile discs<sup>22</sup> and which have potential for use in neuromorphic computing.<sup>4</sup> AIST is sometimes referred to as Ag-In-doped Sb<sub>2</sub>Te, as many alloys are primarily Sb<sub>2</sub>Te, with minor additions of Ag and In that stabilize the amorphous film at low temperatures without compromising rapid crystallization at high temperatures. Here a more Sb-rich composition, nominally Ag<sub>3</sub>In<sub>4</sub>Sb<sub>76</sub>Te<sub>17</sub>, is used. It has an A7 crystal structure,<sup>23</sup> like that of pure Sb, with random substitution of the components on the 6(c) site at temperatures below 600 K and when laser crystallized.<sup>24</sup> AIST alloys are growth-dominated PCMs meaning they have relatively low nucleation rate, *I*, and a high crystal growth rate, *u*, under the conditions used to crystallize bits in memory devices.

The crystal growth rate may be measured through indirect or direct methods. Direct methods based on microscopy enable the identification and tracking of individual crystalline grains in an amorphous material in a series of images allowing independent and unambiguous quantification of u and I. At temperatures well below  $T_g$ , crystallization of solid amorphous PCMs proceeds slowly enough ( $u < 1 \mu m/s$ ) that u may be measured with visible light microscopy,<sup>17</sup> transmission electron microscopy (TEM),<sup>15</sup> and atomic force microscopy (AFM),<sup>16</sup> as has been done for AIST. For many PCMs,  $T_g$  may be difficult or impossible to observe experimentally due to rapid crystallization, however Kalb *et al.* found that  $T_g \approx 433$  K during DSC with a heating rate of 40 K/min for as-deposited  $Ag_{5.5}In_{6.5}Sb_{59}Te_{29}$ ,<sup>26</sup> an alloy similar to the one used here. The distinction is made that the measurement is for "as-deposited" films because the crystallization kinetics of PCMs may be strongly influenced by intrinsic qualities, such as the degree of short-range ordering

and local chemical ordering, of the amorphous structure. The structure of the amorphous phase is not unique and may be impacted by deposition method and thermal annealing, which in turn impact crystallization kinetics. The changes in amorphous structure induced by the melt-quench process are especially significant and have been shown to dramatically increase nucleation rates in AIST.<sup>27,</sup>

Above  $T_{\rm g}$  crystallization proceeds rapidly, and the fraction crystallized,  $\chi$ , may be tracked with nanosecond-scale resolution by reflectivity<sup>15, 27, 29</sup> and resistivity measurements<sup>30, 31</sup> which exploit the high contrast in optical and electrical properties between the amorphous and crystalline phases. Ultrafast DSC12, 32 and synchrotron radiation29 may also be used to extract  $\chi$ . They may be convenient to implement, and these indirect measurements of crystallization can have very high temporal resolution, but separation of the contributions of u and I to  $\chi$  generally requires assumptions about the mode of nucleation and the dimensionality of growth. However, in an elegant experiment by Salinga et al., 15 u was measured (nearly) directly in Ag<sub>4</sub>In<sub>3</sub>Sb<sub>67</sub>Te<sub>26</sub> from 418 K and 553 K using laser reflectivity. The experiment exploited the low nucleation rate of this growth-dominated PCM and the change in reflectively of melt-quenched amorphous marks in a crystalline film was measured with the substrate heated to different temperatures. It was assumed that growth proceeded from the edge of the crystalline AIST with no nucleation events. This assumption was verified by post-mortem TEM after an in-situ experiment for one temperature. A remarkable Arrhenius dependence all the way up to a substrate temperature of 553 K was observed. The growth rate data was used to calculate  $\eta(T)$  and the melt-quenched AIST was found to have an extremely high kinetic fragility (m  $\approx$  135) described in more detail below.

#### 2.2 Crystallization kinetics and viscosity in PCMs

In the classical theory, the growth of a spherical crystalline cluster of radius, r, may be expressed as: $^{33,34}$ 

$$u = \frac{dr}{dt} = \frac{16D}{\lambda^2} \left(\frac{3V}{4\pi}\right)^{\frac{1}{3}} \sinh\left[\frac{V}{2k_B T} \left(\Delta G_v - \frac{2\sigma}{r}\right)\right] = \frac{16}{\lambda^2} \left(\frac{k_B T}{6\pi\eta}\right) \sinh\left[\frac{V}{2k_B T} \left(\Delta G_v - \frac{2\sigma}{r}\right)\right]$$
(1)

where D is the diffusivity,  $\lambda$  is jump distance at the interface, V is the volume of a molecular unit,  $\Delta G_v$  is the Gibbs free energy difference between the crystalline and amorphous phase per unit volume, and  $\sigma$  is the specific interfacial energy between the liquid and crystalline phases. On the right-hand side of EQN. (1), the Stokes-Einstein relation has been used to re-write D in terms of

viscosity,  $\eta$ . With decreasing temperature, D (and the term including  $\eta^{-1}$ ) decreases, whereas the term in the square brackets associated with thermodynamic driving force increases, giving rise to a maximum growth rate,  $u_{max}$  at an intermediate temperature between  $T_g$  and  $T_m$ , as shown schematically in FIG. 1(a). Using EQN. (1), one may derive any one of the three parameters u,  $\Delta G$ , or  $\eta$ , from the other two, however it is challenging to measure them for PCMs between  $T_g$  and  $T_m$ .

The temperature-dependent viscosity,  $\eta(T)$ , of the supercooled liquid plays an important role in determining u(T). In good glass-formers,  $\eta(T)$  has a near Arrhenius behavior, such that  $\log(\eta)$  plotted against 1/T forms a straight line between  $T_g$  and  $T_m$  as seen for  $SiO_2$  in FIG. 1(b) (adapted from [12, 35]), which is termed an Angell plot.<sup>35</sup> Some glass formers deviate from an Arrhenius dependence of  $\eta$  as  $T_g$  is approached from above. This deviation, called the kinetic fragility, is defined as

$$m = [\partial \log_{10} \eta / \partial (T_g/T)]_{T=T_g}.$$
 (2)

Good glass formers have a low fragility (e.g.,  $SiO_2$  with m = 20) and are called strong liquids. The deviation from Arrhenius behavior manifests as a higher slope in the Angell plot as  $T_g/T \rightarrow 1$ , implying a more rapid drop in viscosity as T increases above Tg, as shown for Na<sub>2</sub>O·2SiO<sub>2</sub> and oterphenyl in FIG. 1(b). The o-terphenyl is an example of a fragile liquid. However, it appears that PCMs may display a fragile-to-strong liquid transition, which was originally discovered in water by Angell.<sup>37</sup> In a fragile-to-strong transition, the high-temperature behavior of the liquid is fragile and transitions to strong behavior as the temperature approaches Tg. Orava et al. used viscometry to measure  $\eta$  above  $T_m$  and DSC to extract the low-T viscosity of  $Ag_{5.5}In_{6.5}Sb_{59}Te_{29}$  and found a fragile-to-strong transition in  $\eta(T)$ . 12, 32 The fragile-to-strong transition was also reported by Wei et al. in  $Ge_{15}Te_{85}$ , and Orava et al. reported a decoupling of u from  $\eta$  in  $Ge_2Sb_2Te_5$  based on indirect measurements of the growth rate through ultrafast DSC. 11 An attempt to extract  $\eta$  by Orava et al. 12 from reflectivity data (Salinga et al. 15) in FIG. 1(b) shows the apparent behavior does not align with expected behavior even when the possibility of a fragile-to-strong transition is considered. Experiments using time-resolved reflectivity<sup>15</sup> and ultra-fast DSC<sup>12</sup> have broadened the temperature range for which the crystallization kinetics of AIST have been characterized, but still leave open questions about the crystallization behavior and the character of the undercooled liquid of PCMs, including the form of  $\eta(T)$  near T<sub>g</sub> and its relationship to u(T).

Simultaneous *in situ* TEM and nanocalorimetry, along with other characterization techniques, may be a means to clarify the relationship between u(T) and  $\eta(T)$ . Since its introduction more than 20 years ago,<sup>39</sup> nanocalorimetry has been used for thermal analysis to measure small energy changes ( $\approx 1$  nJ/K) in small volume specimens including nanoparticles and thin films. Extremely high sensitivity is achieved by minimizing the heat capacity of the sensor itself, by locating a heater on a thin suspended silicon nitride membrane *via* microfabrication. This design has opened the possibility of simultaneous quantitative thermal analysis and TEM observation of the specimen to provide detailed microstructural information that can eliminate the need for assumptions about the modes and the relative contribution of nucleation and growth to crystallization. Simultaneous nanocalorimetry and TEM has been used to study rapidly propagating phase transformations with devices designed and fabricated at the National Institute of Standards and Technology (NIST).<sup>40</sup>,

The following work is part of the effort to directly measure u(T) from  $u(T_g)$  to  $u_{max}$ , and to integrate nanocalorimetry with *in situ* TEM. The collection of detailed microstructural information simultaneously with thermodynamic and kinetic data over a broad range of temperatures, including temperatures around where  $u_{max}$  occurs and just above  $T_g$  may help clarify questions around the crystallization kinetics of PCMs, because this is where the data is most grossly lacking. In the following Sections 3.1 - 3.2, DTEM experiments to determine  $u_{max}$  and estimate the maximum observed nucleation rate,  $I_{max}$ , are described as well as more conventional *in situ* TEM experiments for an initial characterization of u near  $T_g$  in as-deposited  $Ag_3In_4Sb_{76}Te_{17}$ . In Section 3.3, those results are placed in context with growth rate data for AIST from the literature and are used to constrain a classical model for nucleation and growth. Sections 3.4 and 3.5 then describe the preliminary results from imaging sub-framing and nanocalorimetry that demonstrate the feasibility of simultaneous direct imaging of crystallization with thermodynamic measurements above  $T_g$ .

#### 3. Results and discussion

#### 3.1 Determination of $u_{max}$ with dynamic TEM

Laser-induced crystallization of 30-nm thick, as-deposited AIST was imaged using DTEM to observe microstructural development and determine  $u_{\text{max}}$ . DTEM is a photoemission TEM technique that uses a laser directed onto the TEM cathode to induce electron emission at precisely controlled times. DTEM is distinguished from other photoemission TEM techniques in that each

photoemitted pulse contains enough electrons to form an image or a diffraction pattern<sup>42</sup> allowing microstructural and crystallographic information during irreversible processes to be gathered with high spatial and temporal resolution. The DTEM at Lawrence Livermore National Laboratory (LLNL) can generate multiple photo-emitted electron pulses spaced over nanoseconds or microseconds. To capture multiple images within several microseconds, a custom-built electrostatic deflector above the TEM projector lenses deflects each image to a different portion of the TEM camera's charge-coupled device, effectively overcoming the camera's refresh rate. Details of the design and operation of DTEM have been described in [<sup>43</sup>] and the references therein. DTEM has been used to study phase transformations in a variety of materials,<sup>44</sup> including crystallization of the PCMs GeTe, <sup>45, 46</sup> Ge<sub>2</sub>Sb<sub>2</sub>Te<sub>5</sub>, <sup>47</sup> and GeSb<sub>6</sub>Te. <sup>10</sup>

A set of DTEM images of AIST crystallization for two experiments conducted with similar specimen laser energies and electron imaging pulse parameters is shown in FIG. 2(a-b). The entire electron transparent window for the specimen in FIG. 2(b) is shown in a TEM image minutes after crystallization is complete in FIG. 2(c). The specimen laser is Gaussian in its spatial profile and heats an oval region since the laser is incident at 42° to the specimen normal. In previous work on GeTe. 46 it was shown that over the duration of such laser heating experiments, the temperature profile established by the specimen laser pulse is established within  $\approx 25$  ns, but it takes many microseconds to decay. Thus, over the few microseconds of the DTEM experiment the local temperature, though non-uniform, is not expected to change significantly except due to heating caused by the release of the enthalpy of fusion at the crystal growth front. In FIG. 2(a-b), both specimens have small grains growing barely at the edge of detection at 100 ns after laser heating. At the laser energies used, the initial grains are nucleated in an oval annulus around the center of the laser heated region and grains grow both inward and outward from this annulus. In FIG. 2(a), both the inward and outward growing crystallization fronts are visible. In FIG. 2(b) inward growth is captured. The relationship between the initial temperature profile and crystallization process and resulting grain structure is shown schematically in FIG. 2(d). A composite TEM image of a lasercrystallized region, FIG. 2(e), shows the change in grain morphology from the edge to the center of the laser crystallized region. The grains that form initially are equiaxed and sub-micron. Using the density of grains in this region,  $I_{max}$  was estimated to be roughly  $10^{12} \,\mathrm{m}^{-3} \,\mathrm{s}^{-1}$  ( $10^{18} \,\mathrm{cm}^{-3} \,\mathrm{s}^{-1}$ ). As growth proceeds outward, almost no nucleation events occur, resulting in columnar grains that end when the crystallization quenches in cooler regions of the sample. The inward growth front is more

irregular and stable grains (infrequently) nucleate and grow in the hotter central portion of the laser-heated region. The resulting grains are roughly equiaxed and many microns across.

The AIST growth rate is plotted as a function of delay time, the time since the specimen laser pulse, for multiple specimen pulse energies in FIG. 3(a-b). The growth rate data is divided into two groups depending on whether the growth rate measured was from (a) crystalline-amorphous interface growing outward away from the center of the laser-heated region (down the local temperature gradient established by the laser) or (b) inward (up the temperature gradient). In both directions, u drops off with increasing time. For outward growth, this is attributed to the reduction in atomic mobility as the local temperature of the substrate drops. The outward growth rate varies with time (and position) in the first microsecond, but then the change in u decreases monotonically, which may be due to the lack of nucleation events and the relatively smooth convex shape of the outward growth front. For inward growth, the drop in u may be attributed to a decrease in the driving force as the temperature approaches T<sub>m</sub>. There is greater variability in u with time during inward growth, which may be attributed to the roughness of the amorphous/crystalline interface and nucleation events ahead of the growth front. As grains grow toward each other, the enthalpy of fusion released may cause a large local increase in temperature, slowing local growth. The eventual impingement of grains, followed by free inward growth may then cause a subsequent increase in u.

Because there is a continuous temperature gradient established by the specimen laser and u drops off in both directions of that gradient, it is assumed the temperature at which  $u_{max}$  occurs is sampled. It is also assumed, based on results of classical nucleation theory, that  $u_{max}$  does not occur at the same temperature as the maximum nucleation rate, as it generally occurs at a higher temperature. Although u in either direction exceeds 22 m/s, the maximum observed growth rate is 23.3 m/s, which occurred in the outward growth, which is discussed in Section 3.3. The higher value is also used as  $u_{max}$  as a constraint for the growth model in Section 3.3.

The  $u_{max}$  for as-deposited AIST is similar to the highest growth rates measured in very similar DTEM experiments<sup>10</sup> on GeSb<sub>6</sub>Te (equivalently Ge<sub>12.5</sub>Sb<sub>75</sub>Te<sub>12.5</sub>) which has a similarly high Sb content to Ag<sub>3</sub>In<sub>4</sub>Sb<sub>76</sub>Te<sub>17</sub>. In those experiments  $u_{max}$  was not reported, the maximum observed growth rate in as-deposited GeSb<sub>6</sub>Te was 10.8 m/s and growth exceeding 17.8 m/s was observed for one specimen that had been pre-annealed with a sub-threshold laser pulse. These growth rates

in Sb-rich AIST and GeSb<sub>6</sub>Te far exceed the maximum reported growth rates of 3 m/s for Ge<sub>2</sub>Sb<sub>2</sub>Te<sub>5</sub><sup>11</sup> and 3.8 m/s for GeTe.<sup>46</sup>

#### 3.2 In situ TEM with furnace-style heating holder

For initial measurements of u near T<sub>g</sub> (from 413 K to 443 K) on 30-nm thick, as-deposited AIST, a furnace-style Gatan 652 heating holder was used with the I<sup>3</sup>TEM at the Center for Integrated Nanotechnologies (CINT) at Sandia National Laboratories (SNL). The high end of this range is 10 K above the reported T<sub>g</sub> for as-deposited Ag<sub>5.5</sub>In<sub>6.5</sub>Sb<sub>59</sub>Te<sub>29</sub>. The spatial resolution and fast, direct-electron-detection camera enabled imaging of rapidly growing grains before impingement in a temperature range slightly higher than what was reached with recent in situ optical microscopy experiments.<sup>17</sup> Above 443 K, data were not collected because nucleation and growth to impingement occurred too rapidly. Although Tg is sensitive to stoichiometry as well as other factors such as heating rate, these measurements are approaching (and may exceed) Tg for the alloy used in these experiments. Growth was initially tracked from a crystalline edge that had been prepared before the in-situ heating by condensing the electron beam on the as-deposited amorphous film and translating the sample to form a straight crystalline edge, which is still visible on the left side of FIG. 4(a). This obviated the need to wait for a nucleation event to start a growing crystal front, however, in time nucleation events occurred ahead of the pre-crystallized region. Growth out from the pre-crystallized edge was uniform, whereas nucleated grains had either jagged or smooth fronts depending on the temperature, this is shown in frames from low magnification videos in FIG. 4(a-b). Videos of crystallization at higher magnification used for growth rate measurements are available in the Supplemental Materials as well as example frames in FIG. S2. The growth rate data are plotted in FIG. 5(a). The measured rates fall at somewhat higher temperatures compared to data from in situ optical microscopy heating experiments on asdeposited thin films with the same nominal composition.<sup>17</sup> This may be due to thermal lag causing a small difference in temperature between the region of interest and the thermocouple within the TEM heater.

For the purposes of the growth model in Section 3.3, *u* measured at and above 433 K are taken to be in the supercooled liquid.

#### 3.3 Modelling crystal growth

FIG. 5(a) shows growth rate data from the *in situ* TEM experiments on Ag<sub>3</sub>In<sub>4</sub>Sb<sub>76</sub>Te<sub>17</sub>, isothermal growth rate data from optical microscopy experiments on thin films with the same thickness and stoichiometry,<sup>17</sup> and data for similar AIST alloys measured with atomic force microscopy (AFM),<sup>16</sup> and laser reflectivity.<sup>15</sup> EQN. (1), the function for *u*(T), is fitted to the data for Ag<sub>3</sub>In<sub>4</sub>Sb<sub>76</sub>Te<sub>17</sub> along with the steady state nucleation rate, *I*<sup>ss</sup>, given by the following equation:<sup>34</sup>

$$I^{SS} = \frac{4\gamma n_c^{2/3} Z}{V} exp\left(-\frac{V\Delta G_c}{k_B T}\right)$$
 (3)

where  $\gamma$  is the jump frequency,  $n_c$  is the number of monomers in a critical cluster given by  $[(32\pi\sigma^3)/(3V\Delta G_v^3)]$ , Z is the Zeldovich factor given by  $[\Delta G_v V/(6\pi k_B T n_c)]^{1/2}$ , and  $\Delta G_c$  is the critical value of  $\Delta G_v$  for the formation of a stable nucleus. Following Senkader *et al.*,<sup>34</sup> the temperature dependence of  $\Delta G_v$  is related to the molar enthalpy of fusion,  $\Delta h_f$ , by:

$$\Delta G_{v} = \frac{\Delta h_{f}}{v_{m}} \frac{T_{m} - T}{T_{m}} \left( \frac{7T}{T_{m} + 6T} \right) \tag{4}$$

where  $v_m$  is the molar volume. The Mauro-Yue-Ellison-Gupta-Allan (MYEGA) equation is used for the temperature-dependent viscosity and may be written in the form:<sup>32, 48</sup>

$$log_{10}\eta(T) = log_{10}\eta_{\infty} + (12 - log_{10}\eta_{\infty}) \frac{T_g}{T} exp\left[\left(\frac{m}{12 - log_{10}\eta_{\infty}} - 1\right)\left(\frac{T_g}{T} - 1\right)\right] (5)$$

where  $\eta_{\infty}$  is the high temperature limit of the viscosity and m is the kinetic fragility as defined in EQN. (2). This form of the MYEGA equation has been applied to model the temperature-dependent viscosity in an AIST alloy by Salinga *et al.*<sup>15</sup>

Equations (1) and (3) were fitted to the two *in situ* TEM measurements of u nominally at and above  $T_g$  and the DTEM measurements of  $u_{\text{max}}$  and  $I_{\text{max}}$ . Data from the DTEM experiments are represented as horizontal bars in FIG. 5 since the temperature cannot be measured *in situ* and cannot be modelled with the desired accuracy, however the data still provide constraints for fitting the equations. The growth and nucleation equations have nine parameters, six of which were set to fixed values, shown in TABLE 1. The grain radius was chosen to be 1  $\mu$ m, roughly the size of the grains observed in the in-situ TEM crystallization experiments presented here. The jump distance,  $\lambda$ , was approximated as the nearest neighbor distance in the liquid. The interfacial energy,  $\sigma$ , in EQNs. (1) and (3) and  $T_g$  and m in EQN. (5) were used as free fitting parameters. Their initial

values are in TABLE 2, together with the literature sources producing these values. At this grain size, the resulting growth rate is largely independent of the interfacial energy, and increasingly so with grain growth. In contrast, the nucleation rate depends exponentially on the cube of the interfacial energy, so the measured  $I_{max}$  largely determines the fitted interfacial energy. The fitted values of the free parameters resulting from the optimization process, shown in TABLE 2, were used to generate plots of crystal growth rate and nucleation rate shown in FIG. 5(a) and (b).

Of the three free parameters used for fitting, the fragility, m, and the glass transition temperature,  $T_g$ , appear exclusively in the functional form of the viscosity. The fragility largely determines the slope of the change in the logarithm of the growth rate near  $T_g$ . The high temperature limit of the viscosity,  $\eta_{\infty}$ , is the third constant in the EQN. (5) and a candidate fitting parameter, but its fit has a stronger influence at higher temperature and thus on the fit to the experimentally-determined  $u_{max}$ . Both  $T_g$  and  $\eta_{\infty}$  are subject to significant uncertainty, but  $T_g$  must be well determined to within a few degrees for a high-quality fit of the growth rate data near  $T_g$ , while  $\eta_{\infty}$  can vary by an order of magnitude with the model remaining consistent with the qualitative behavior observed experimentally, and the fitted parameters physically plausible. To illustrate this difference, a fit was attempted, using fixed  $T_g$  of 433K and free  $\eta_{\infty}$ , that resulted in a non-physical fragility of 500. Additionally, unlike  $\eta_{\infty}$ ,  $T_g$  may depend on the details of the amorphous state, so literature values should not be expected to match the specific films used for these experiments with great accuracy. For these reasons,  $T_g$  was used as a free parameter instead of  $\eta_{\infty}$ .

Fitting against only the final two data points of the TEM crystallization results presented here, and  $u_{max}$  and  $I_{max}$  measured by the DTEM only barely constrain the three free parameters of the model. As a consequence the standard error is large, as shown in TABLE 2, and is strongly dependent on the amount of data available for the fit. Removing just one of the constraints increases the standard error in the free parameters by orders of magnitude. Similarly, even a small amount of additional data beyond  $T_g$  should significantly reduce the standard error in the parameters.

As explained above, the nucleation rate is much more sensitive to the interfacial energy than the growth rate, so the interfacial energy can be fit to the maximum nucleation rate freely. The viscosity parameters depend on all the data, which may not all be wholly compatible with the model and, as a consequence, not all constraining data can be satisfied equally well. Since there is

more growth rate data in the low temperature regime, the overall error was minimized at the cost to the fit to the maximum growth rate, measured to be 23 m/s with the DTEM whereas the model predicts 7 m/s. The discrepancy could be a consequence of some inadequacy of the viscosity model. While the model used here does account for the fragility of AIST, its failure to fit against the maximum growth rate suggests that it fails to match the physical viscosity environment between  $T_g$  and  $T_m$ . Similarly, inadequacy of the functional form of  $\Delta G_{\nu}(T)$  could limit the fit. All this speaks to the need for more and better measurements of u(T),  $\eta(T)$ , and  $\Delta G_{\nu}(T)$ , especially immediately above  $T_g$ . The path for making such measurements is described in 3.4 and 3.5.

According to this classical model the maximum steady state nucleation rate,  $I_{max}^{ss}$ , occurs at 514 K. In the DTEM experiments,  $u_{max}$  occurs in outward growth from the region with the highest nucleation rate, down the temperature gradient and FIG. 5(a) indicates the growth below 514 K would be orders of magnitude below the observed  $u_{max}$ . This is because the temperature of the propagating amorphous/crystalline interface is determined both by the temperature established by laser heating as well as  $\Delta h_f$  released at the growth front, with the 10-nm silicon nitride membrane providing only a modest thermal sink. Modeling of the temperature at the interface is beyond the scope of this work, but a simple estimate of the potential temperature rise at the interface caused by the phase transformation may be made using  $\Delta h_f$  for AIST (Table 1) and the heat capacity,  $c_p$ , of AIST and amorphous silicon nitride. The heat capacity, cp of AIST has not been reported, but to estimate it for this very Sb-rich alloy, we take cp of liquid Sb, 260 J/(kg·K). For amorphous silicon nitride, cp at TRT has been reported as 400 J/(kg·K).<sup>49</sup> Assuming that a thin layer of liquid AIST crystallizes and rejects  $\Delta h_f$  into a layer of similar width of the AIST liquid ahead of the front as well as the supporting silicon nitride, a local rise in temperature of > 400 K may occur. This is more than adequate to raise the temperature into the region of maximal growth. Also enough for the inward growth to cause enough heating of the film to destabilize it and cause dewetting, as seen in FIG. 2(c), visible as bare white spots near the center of the crystallized region.

#### 3.4 In situ TEM with laser heating and sub-framed imaging

To image crystallization at temperatures well above T<sub>g</sub>, in addition to high spatial and temporal resolution, high heating rates are necessary to rapidly by-pass lower temperature crystallization events. To bypass crystallization at lower temperatures, heating was induced with multiple laser pulses directed on the as-deposited AIST and an Integrated Dynamic Electron Solutions (IDES)

Inc. Relativity electrostatic sub-framing system,<sup>20</sup> similar to the electrostatic deflector in the LLNL DTEM, installed on the I<sup>3</sup>TEM at the CINT was used to image crystal growth at a rate of 1 sub-frame per millisecond. This system operates by using a field-limiting aperture and a fast (switching time on a scale of tens of ns) electrostatic deflection system to subdivide a large camera into subframes. The timing system that controls the deflection system also controls the sample drive laser, allowing laser-driven processes to be captured in burst-mode multi-frame "movies" with kHz-scale frame rates.

The temperature could not be reliably determined, but the goal of these experiments was to demonstrate that a propagating growth front could be imaged with adequate spatial resolution and acceptable signal-to-noise ratio accessing T-u space between experiments with more conventional low temperature  $in \, situ$  microscopy and high temperature DTEM experiments. FIG S1 shows four sequential sub-frames during laser-heating induced growth. The images are noisy, but more than adequate to determine that  $u = 3.4 \times 10^{-5} \, \text{m/s} \pm 3.2 \times 10^{-6} \, \text{m/s}$ . The uncertainty is one standard deviation of the mean of u averaged over the length of the visible growth front. This is more than an order of magnitude higher u than what has been determined by other microscopic techniques (excluding the DTEM), c.f. FIG. 5. This experiment was performed in a TEM with a LAB6 thermionic emitter source, so it is expected that growth may be imaged for higher T and u with a brighter source, such as a field emission gun, enabling detailed microstructural characterization of crystallization for a range of temperatures above  $T_g$ . However, the accessible u(T) depends not only on the technological capabilities (imaging frame rate and controlled heating rate), but also on the nucleation and growth rates, which control ultimate scale of the grain size, and the specimen contrast.

These laser-driven experiments were not pursued further for the present study, because the temperature of the laser heated specimen could not be determined adequately. Rather, they serve as proof-of-principle measurements demonstrating the ability to capture front propagation rates in the mid- $10^{-5}$  m/s range using electrostatic sub-framing. For the DTEM experiments, the uncertainty in the temperature caused by laser heating was acceptable, because  $u_{\text{max}}$  was determined, which has value in constraining growth rate models even if the temperature is not known. But in the range just above  $T_g$ , growth rate measurements only constrain the fit if they may be associated with a well-known temperature or heating rate. There are other means of rapidly heating PCMs during *in situ* imaging. Commercially-available, microfabricated, "chip-based" *in* 

situ heaters designed for TEM holders can be heated rapidly to 1200 °C, however uniformity, reproducability, and measurement of the temperature in the region of interst can still be a limitation in experiments where the temperature must be well-determined, especially when high heating rates are required. These issues may be addressed by using nanocalorimetry devices, described below, which although also based on a microfabricated chip platform, are designed and individually calibrated specifically for uniform temperature measurement and control and which provide a means for quantitative measurement of thermal properties. <sup>50, 51</sup>

#### 3.5 Nanocalorimetry

In this preliminary study performed at the NIST, six microfabricated nanocalorimeters were used to study the crystallization of as-deposited AIST at four heating rates. Schematics of the nanocalorimeter are shown in FIG 6.(a-b). The platinum film plays the simultaneous role of four-point probe and heater. To enable simultaneous TEM observations the Pt heater has three windows etched into it, which have been optimized for size without compromising thermal uniformity.<sup>40</sup> After calibration of the nanocalorimeter, the electrical measurements can be used to determine the temperature of the heater. The large silicon nitride window is extremely delicate but is necessary to thermally isolate the sample during the calorimetry experiments. The specimen is deposited onto the silicon nitride side of the nanocalorimeter, as shown in the side view, to prevent shorting the four-point Pt probe. Since crystallization could not be reversed by melt-quenching in these experiments, each calorimeter was used only once. To test the reproducibility of the results, two devices were used to repeat the experiment for two different heating rates.

The preliminary results of the four heating rates are shown together in FIG 6.(c). The data for the repeated experiments lie on top of each other, indicating excellent reproducibility. The prominent peaks in the heating rates are caused by the exothermic crystallization event. Consistent with previous DSC results,<sup>12</sup> the peak temperature,  $T_p$ , shifts to higher temperatures with increased heating rate. The onset heating rate,  $\phi$ , is defined by the heating rate just preceding the peak. This heating rate was determined for each experiment using the derivative of the heating rate with respect to temperature, though other derivatives, such as one with respect to time, could be suitable. The derivative of the heating rate is relatively flat, so its median value closely tracks the base surrounding the peak. The onset temperature was defined by the first temperature on the low

temperature side of the peak at which the derivative of the heating rate is less than the median value and  $\phi$  was as taken to be the average of the 20 data points preceding this onset temperature.

Using the onset heating rates and the peak temperatures a Kissinger analysis  $^{12}$  was run, the results of which are shown in FIG. 6(d). The activation energy for crystallization,  $E_x$ , from the Kissinger analysis is shown in TABLE 3 along with the activation energy for crystal growth,  $E_{cg}$ , from isothermal growth experiments. The Arrhenius plots for these data are available in FIG. S3 of the Supplementary Material.  $E_x$  derived from the calorimetry experiments agrees reasonably with  $E_{cg}$  for growth derived from isothermal *in situ* optical microscopy experiments on asdeposited AIST with the same nominal composition.  $E_x$  convolves contributions from both nucleation and growth and thus may been expected to be greater than,  $E_{cg}$ . The activation energies are close, even though the temperatures at which crystallization occurs in the nanocalorimetry experiments is considerably higher. Based on the reported  $T_g$  for AIST, the optical experiments are measuring a solid-solid phase transformation and the calorimetry is measuring crystal growth from the undercooled liquid. This is not unlike the strictly Arrhenius growth observed by Salinga *et al.* in the reflectivity measurements that also span  $T_g$ .

These initial nanocalorimetry results use devices designed to be used in a TEM and are very promising in terms of reproducibility and potential for accessing even higher heating rates and crystallization temperatures. When combined with spatio-temporal resolution offered by subframing on a direct electron detection camera, the region above  $T_g$  should become accessible for direct measurement of u(T) and  $\Delta h_f$ . Any physical model of the crystallization kinetics above  $T_g$  requires information about the driving force,  $\Delta G_v(T)$ , and the temperature-dependent viscosity,  $\eta(T)$  which are challenging to measure far below  $T_m$  in AIST and other PCMs, because they crystallize so quickly. As described in section 3.3, the lack of data for AIST is a limiting factor in the ability to fit to the classical model for nucleation and growth. This lack of data similarly limits the ability to test models for any PCM. A rapid, reliable means to measure u(T) and collect quantitative thermodynamic data above  $T_g$  is expected to improve the fundamental understanding of PCM crystallization kinetics which will support development of new memory devices.

# 4. Summary and conclusions

The paucity of data spanning the very large range of velocity scales is a limiting factor in modelling growth of the crystalline phase in PCMs. In these experiments, we have explored

multiple methods for addressing this problem. DTEM experiments were used to determine  $u_{max}$  and estimate  $I_{max}$  for thin films of as-deposited Ag<sub>3</sub>In<sub>4</sub>Sb<sub>76</sub>Te<sub>17</sub>. This data, along with other growth rate data for isothermal growth near T<sub>g</sub>, was used to fit to a classical model for crystal growth. It was demonstrated that imaging of crystal growth above T<sub>g</sub> may be performed with currently available electron microscopy technology. Preliminary calorimetry results were presented from nanocalorimeters designed for experiments enabling simultaneous TEM imaging in a range about T<sub>g</sub>. These planned experiments may reveal limits on the interpretation of previous experiments due to lack of information about the microstructural details of the phase transformation. They may show that previously unexplained behavior falls into current descriptions of glass-forming behavior, or it may confirm that the relationship between temperature-dependent viscosity and growth in PCMs requires re-evaluation.

#### 5. Methods

#### 5.1 Specimen preparation for *in-situ* TEM experimental methods

Amorphous AIST for DTEM and sub-framed TEM experiments was deposited at T<sub>RT</sub> using DC magnetron sputtering onto two types of commercially-available TEM specimen supports: ones with nine 10-nm thick amorphous silicon nitride windows (Norcada TA301Z) and one with carbon-coated Formvar supported by a 200 mesh Cu grid. Sputtering was performed with a 2" inch diameter target (Kurt J. Lesker Co.) with a composition of Ag<sub>3</sub>In<sub>4</sub>Sb<sub>76</sub>Te<sub>17</sub> (impurities: 30 parts per million (ppm) C, 9 ppm Cu, 4 ppm Fe, 9 ppm Si, 2 ppm W) using 5 W DC power, and an Ar (99.999% pure) pressure of 0.4 Pa (3 mTorr) for 1440 s to achieve 30 nm films.

#### **5.2 Dynamic TEM methods**

Laser crystallization experiments using a single laser pulse for specimen heating were performed in the DTEM at LLNL on thin films deposited on the silicon nitride supports. Crystallization was induced with 1.2  $\mu$ J to 2.2  $\mu$ J pulses from a frequency doubled Nd:YAG laser (532 nm wavelength, spatially Gaussian with (90  $\pm$  5)  $\mu$ m 1/e² diameter, temporally Gaussian 12 ns FWHM duration), directed onto the specimen  $\approx$  42° from the specimen normal. Bright-field TEM images of each crystallization event were generated from nine electron pulses. The pulse duration and temporal spacing between the pulses was varied to resolve different stages of the crystallization process. Experiments were performed with 50 ns pulses and either a 200 ns, 500 ns,

or 1000 ns interframe space or with a 20 ns pulses with an interframe spacing of 100 ns. The delay between the specimen laser and the first electron image varied from 0 ns to 3000 ns.

TEM images of the crystallized AIST after the *in-situ* experiments were taken with the DTEM operate in thermionic emission mode and with an FEI Titan TEM operated at 200 keV.

The growth rate was measured for 32 separate DTEM crystallization experiments. The inward and outward growth from the initial crystalline annuli were separated during analysis due to their distinct temperature profiles, as shown in FIG. 2(d). Each experiment yielded an image with, at most, nine subframes showing a crystallization front. The interframe time between subframes varied between 100 ns and 1000 ns but was fixed for each individual experiment. Due to the low S/N and variation in subframe positioning, some parts of the image analysis were performed manually. Image processing involved placing each sub-frame it on its own layer in an image stack and registering each sub-frame to the previous sub-frame by eye. New layers were created on which the amorphous/crystal boundary were traced by hand. The traced layers were processed with a program that calculated the u using the manually drawn edges, interframe time, and pixel scale. Since the manually drawn interfaces were not single pixel lines, the central axis of the interface was calculated by skeletonization. For each pixel in the skeletonized interface, the nearest point on the previous frame was determined by calculating all distances from a given pixel to the previous edge and choosing the minimum. This approach is inefficient, but produces acceptable program runtimes, given the small scale of the problem. The number of measurements that went into each value of u in FIG. 3 varied with the visible length of the growth front, but the median number was 564. The average displacement per frame was calculated from the list of nearest pixels, then u was calculated from the displacement by scaling by the interframe time and pixel scale. The error bars in FIG. 3 represent a conservative (worst case) estimate of the largest source of error: the manual determination the interface position, which is a factor of ten larger than the standard deviation of the mean of the measurements for each time step.

#### 5.3 In situ TEM with a "furnace-style" heater

Crystallization experiments were performed using the I<sup>3</sup>TEM at the Center for Integrated Nanotechnologies at Sandia National Laboratories using AIST deposited on the carbon-coated Formvar TEM grids. The I<sup>3</sup>TEM is a JEOL 2100 TEM equipped with a variety of commercially-available and custom-built *in situ* capabilities. In one set of experiments, a single specimen was heated using a Gatan 652 heating holder to measure isothermal crystal growth from 413 K to

443 K. A fully visible square in the Cu grid closest to the thermocouple in the holder heating element was chosen for the experiment to ensure that the temperature of the specimen in the region imaged was close to the measured temperature. An edge of the AIST in the grid square was precrystallized using the condensed electron beam to eliminate the need to nucleation and to set the initial region of interest (ROI), the crystal-amorphous boundary. To attain the fastest heating to the isothermal set points, the set points were input manually, and the holder was allowed to heat at its maximal rate. It took 130 s to reach and stabilize at 413 K from  $T_{RT}$ , then a  $\approx$  120 s video of growth was collected with a TVIPS Fastscan-F114TR 1k × 1k camera at a frame rate of 15 frames per second. The specimen was then heated to 423 K in 20 s and video collected at that temperature. It was then heated to 433 K and 443 K. In both cases, it took 15 s to reach the set point at which the video was collected. An image analysis algorithm was written in-house using scikit-image to analyze each frame of the TVIPS videos. The amorphous-crystalline interface for each frame was identified via over-segmentation, then smoothing. Over-segmentation is suitable for segmenting these images since the crystalline and amorphous regions are distinguished by a difference in texture, not average brightness. For each pixel of an interface, the nearest pixel on the next frame was determined. The average growth rate between a pair of frames was then calculated from the average displacement between these pairs of closest pixels. Repeating this process for each frame results in a sequence of growth rates, the average of which is the reported growth rate for a given temperature. The standard deviation of the mean of the sequence of growth rates is the reported uncertainty.

#### 5.4 In situ TEM with laser heater and sub-framed imaging

An AIST film deposited on a Cu grid was heated *in situ* using a 20 W SPI G4 1064 nm fiber-based laser with 36-ns laser pulses firing at 33 kHz and a setpoint intensity of 70 parts/1000. TEM imaging was performed at 200 keV and images were recorded with a TVIPS F415-MP 4k × 4k camera. Sixteen sub-frames were captured in each image using the IDES electrostatic deflector. One subframe is a sacrificial beam-blanker frame (as described in [<sup>20</sup>]) while the remaining 15 subframes are exposed in sequence, 1 ms each, for a total of 15 ms. Starting immediately after the first subframe, the laser was gated on for 7 ms, thus locally heating the area of interest with 231 laser pulses. The laser was then off for the remaining 7 ms of exposure. The growth rate was found

using manual sub-frame alignment, and edge tracing and interface displacement were calculated from the tracing as described for the DTEM data.

#### 5.5 Nanocalorimetry methods

The nanocalorimeters used for the AIST crystallization experiments were fabricated at the NIST CNST. Each sensor was individually calibrated to determine its temperature as a function of resistance. The results of the calibration are the three coefficients of a second order polynomial fit to the collected temperature against resistance data. To accurately measure the heat capacity of the sample as a function of temperature, a baseline measurement was performed on each empty nanocalorimeter. The baseline measurements were conducted at 4 mPa (3 x 10<sup>-5</sup> Torr) to approximate conditions inside the TEM during future *in-situ* experiments.

Amorphous AIST thin films were deposited onto the calibrated nanocalorimeters at T<sub>RT</sub> using RF sputtering at the NIST CNST. Sputtering was performed with UHP (99.999% pure) Ar at 200 W for 90 s with a 3" diameter target (MSE Supplies LLC.) with a nominal composition of Ag<sub>3</sub>In<sub>4</sub>Sb<sub>76</sub>Te<sub>17</sub>, which resulted in an approximately 30 nm thick film. A shadow mask was used during deposition to confine the deposited film to the effective heater area. The calorimetry experiments were run at the same heating rate and vacuum conditions as those used for the baseline measurement. Details of fabrication, calibration, and operation of these devices have been described in detail elsewhere.<sup>51</sup>

# **Acknowledgments**

Effort by M.K.S. and I.M. was supported by the National Science Foundation, Division of Materials Research CER [Grant No. 1945520]. TEM was performed at the Oregon State University Electron Microscope Facility which is sup-ported by NSF MRI Grant No. 1040588, the Murdock Charitable Trust, and the Oregon Nanoscience and Micro-Technologies Institute. M.K.S would like to thank Dr. John Roehling and Dr. Garth Egan for assistance with thin film deposition and DTEM experiments at LLNL. Portions of this work were performed under the auspices of the U.S. Department of Energy by Lawrence Livermore National Laboratory. Lawrence Livermore National Laboratory is operated by Lawrence Livermore National Security, LLC., for the U.S. Department of Energy, National Nuclear Security Administration under Contract No. DE-AC52-07NA27344. Work was performed at the Center for Integrated Nanotechnologies, a User Facility operated for the U.S. DOE Office of Science at Sandia National Laboratories (SNL), managed and operated by National Technology & Engineering Solutions of Sandia, LLC, a wholly owned subsidiary of Honeywell International, Inc., for the U.S. DOE's National Nuclear Security Administration under contract DE-NA-0003525. This work was performed under the Laboratory Directed Research and Development program at SNL. This material is based in part upon work supported by the U.S. Department of Energy, Office of Science, Office of Basic Energy Sciences, under Award No. DE-SC0013104. Views expressed here do not necessarily represent the views of

the U.S. DOE or U.S. Government. Research performed in part at the NIST Center for Nanoscale Science and Technology. Any mention of commercial products is for information only; it does not imply recommendation or endorsement by the NIST.

# **Data Availability**

The datasets generated during and analyzed during the current study are available from the corresponding author on reasonable request.

#### References

- 1. S.R. Ovshinsky: Reversible electrical switching phenomena in disordered structures. *Physical Review Letters*. **21**(20), 1450 (1968).
- 2. M. Chen, K.A. Rubin and R.W. Barton: Compound materials for reversible, phase-change optical-data storage. *Appl. Phys. Lett.* **49**(9), 502 (1986).
- 3. Y.V. Pershin and M. Di Ventra: Memory effects in complex materials and nanoscale systems. *Advances in Physics*. **60**(2), 145 (2011).
- 4. W. Zhang, R. Mazzarello, M. Wuttig and E. Ma: Designing crystallization in phase-change materials for universal memory and neuro-inspired computing. *Nature Reviews Materials.* **4**(3), 150 (2019).
- 5. Y.B. Li, Z.R. Wang, R. Midya, Q.F. Xia and J.J. Yang: Review of memristor devices in neuromorphic computing: materials sciences and device challenges. *J. Phys. D-Appl. Phys.* **51**(50), 503002 (2018).
- 6. N. Yamada, E. Ohno, K. Nishiuchi, N. Akahira and M. Takao: Rapid-phase transitions of GeTe-Sb<sub>2</sub>Te<sub>3</sub> pseudobinary amorphous thin-films for an optical disk memory. *J. Appl. Phys.* **69**(5), 2849 (1991).
- 7. V. Weidenhof, N. Pirch, I. Friedrich, S. Ziegler and M. Wuttig: Minimum time for laser induced amorphization of Ge<sub>2</sub>Sb<sub>2</sub>Te<sub>5</sub> films. *J. Appl. Phys.* **88**(2), 657 (2000).
- 8. S.R. Elliott: Chalcogenide phase-change materials: past and future. *International Journal of Applied Glass Science*. **6**(1), 15 (2015).
- 9. J. Orava and A.L. Greer: Fast crystal growth in glass-forming liquids. *Journal of Non-Crystalline Solids*. **451**, 94 (2016).
- 10. M.M. Winseck, H.-Y. Cheng, G.H. Campbell and M.K. Santala: Crystallization kinetics of the phase change material GeSb<sub>6</sub>Te measured with dynamic transmission electron microscopy. *Dalton Transactions*. **45**, 9988 (2016).
- 11. J. Orava, A.L. Greer, G. B., D.W. Hewak and C.E. Smith: Characterization of supercooled liquid Ge<sub>2</sub>Sb<sub>2</sub>Te<sub>5</sub> and its crystallization by ultrafast-heating calorimetry. *Nat. Mater.* 11, 279 (2012).
- 12. J. Orava, D.W. Hewak and A.L. Greer: Fragile-to-strong crossover in supercooled liquid Ag-In-Sb-Te studied by ultrafast calorimetry. *Adv. Funct. Mater.* **25**(30), 4851 (2015).
- 13. J. Orava and A.L. Greer: Kissinger method applied to the crystallization of glass-forming liquids: Regimes revealed by ultra-fast-heating calorimetry. *Thermochimica Acta.* **603**, 63 (2015).
- 14. B. Chen, J. Momand, P.A. Vermeulen and B.J. Kooi: Crystallization kinetics of supercooled liquid Ge-Sb based on ultrafast calorimetry. *Cryst. Growth Des.* **16**(1), 242 (2016).
- 15. M. Salinga, E. Carria, A. Kaldenbach, M. Bornhoefft, J. Benke, J. Mayer and M. Wuttig: Measurement of crystal growth velocity in a melt-quenched phase-change material. *Nature Communications.* **4**, 1 (2013).
- 16. J. Kalb, F. Spaepen and M. Wuttig: Atomic force microscopy measurements of crystal nucleation and growth rates in thin films of amorphous Te alloys. *Appl. Phys. Lett.* **84**(25), 5240 (2004).
- 17. V.L. Bird: *Crystallization Rates of AIST and Ge Thin Films by Optical and Electron Microscopy*, M.S. thesis, Materials Science (Oregon State University, Corvallis, 2019).
- 18. G. Eising, T. Van Damme and B.J. Kooi: Unraveling crystal growth in GeSb phase-change films in between the glass-transition and melting temperatures. *Cryst. Growth Des.* **14**(7), 3392 (2014).

- 19. M.K. Santala, B.W. Reed, S. Raoux, T. Topuria, T. LaGrange and G.H. Campbell: Capturing irreversible reactions with nanosecond-scale dynamic TEM movies: measuring crystal growth rates during laser annealing of phase change materials. *Microscopy and Microanalysis*. **19**(S2), 1156 (2013).
- 20. B.W. Reed, A.A. Moghadam, R.S. Bloom, S.T. Park, A.M. Monterrosa, P.M. Price, C.M. Barr, S.A. Briggs, K. Hattar, J.T. McKeown and D.J. Masiel: Electrostatic subframing and compressive-sensing video in transmission electron microscopy. *Structural Dynamics*. **6**(5), 054303 (2019).
- 21. H. Iwasaki, M. Harigaya, O. Nonoyama, Y. Kageyama, M. Takahashi, K. Yamada, H. Deguchi and Y. Ide: Completely erasable phase-change optical disc .2. Application of Ag-In-Sb-Te mixed-phase system for rewritable compact disc compatible with CD-velocity and double CD-velocity. *Japanese Journal of Applied Physics*. **32**(11B), 5241 (1993).
- 22. H. Tashiro, M. Harigaya, Y. Kageyama, K. Ito, M. Shinotsuka, K. Tani, A. Watada, N. Yiwata, Y. Nakata and S. Emury: Structural analysis of Ag-In-Sb-Te phase-change material. *Japanese Journal of Applied Physics* 41(6A), 3758 (2002).
- 23. T. Schroder, T. Rosenthal, C. Gold, E.W. Scheidt, W. Schnick and O. Oeckler: Two synthetic approaches to Ag<sub>3.4</sub>In<sub>3.7</sub>Sb<sub>76.4</sub>Te<sub>16.5</sub> bulk samples and their transport properties. *Zeitschrift Fur Anorganische Und Allgemeine Chemie*. **639**(15), 2868 (2013).
- 24. T. Matsunaga and N. Yamada: Crystallographic studies on high-speed phase-change materials used for rewritable optical recording disks. *Japanese Journal of Applied Physics* **43**(7B), 4704 (2004).
- 25. D.J. Sarrach, J.P. DeNeufville and W.L. Haworth: Studies of amorphous Ge-Se-Te alloys (1): preparation and calorimetric observations. *Journal of Non-Crystalline Solids*. **22**(2), 245 (1976).
- 26. J.A. Kalb, M. Wuttig and F. Spaepen: Calorimetric measurements of structural relaxation and glass transition temperatures in sputtered films of amorphous Te alloys used for phase change recording. *Journal of Materials Research.* **22**(3), 748 (2007).
- 27. B.-S. Lee, R.M. Shelby, S. Raoux, C.T. Retter, G.W. Burr, S.N. Bogle, K. Darmawikarta, S.G. Bishop and J.R. Abelson: Nanoscale nuclei in phase change materials: Origin of different crystallization mechanisms of Ge<sub>2</sub>Sb<sub>2</sub>Te<sub>5</sub> and AgInSbTe. *J. Appl. Phys.* **115**(6), 063506 (2014).
- 28. B.S. Lee, G.W. Burr, R.M. Shelby, S. Raoux, C.T. Rettner, S.N. Bogle, K. Darmawikarta, S.G. Bishop and J.R. Abelson: Observation of the role of subcritical nuclei in crystallization of a glassy solid. *Science*. **326**(5955), 980 (2009).
- 29. Y. Fukuyama, N. Yasuda, J. Kim, H. Murayama, Y. Tanaka, S. Kimura, K. Kato, S. Kohara, Y. Moritomo, T. Matsunaga, R. Kojima, N. Yamada, H. Tanaka, T. Ohshima and M. Takata: Time-resolved investigation of nanosecond crystal growth in rapid-phase-change materials: Correlation with the recording speed of digital versatile disc media. *Applied Physics Express.* 1(4), 045001 (2008).
- 30. W.K. Njoroge and M. Wuttig: Crystallization kinetics of sputter-deposited amorphous AgInSbTe films. *J. Appl. Phys.* **90**(8), 3816 (2001).
- 31. W.K. Njoroge, H. Dieker and M. Wuttig: Influence of dielectric capping layers on the crystallization kinetics of Ag<sub>5</sub>In<sub>6</sub>Sb<sub>59</sub>Te<sub>30</sub> films. *J. Appl. Phys.* **96**(5), 2624 (2004).
- 32. J. Orava, H. Weber, I. Kaban and A.L. Greer: Viscosity of liquid Ag-In-Sb-Te: Evidence of a fragile-to-strong crossover. *Journal of Chemical Physics.* **144**(19), 194503 (2016).
- 33. K.F. Kelton and A.L. Greer: Transient nucleation effects in glass-formation. *Journal of Non-Crystalline Solids*. **79**(3), 295 (1986).
- 34. S. Senkader and C.D. Wright: Models for phase-change of Ge<sub>2</sub>Sb<sub>2</sub>Te<sub>5</sub> in optical and electrical memory devices. *J. Appl. Phys.* **95**(2), 504 (2004).
- 35. C.A. Angell: Formation of glasses from liquids and biopolymers. Science. 267(5206), 1924 (1995).
- 36. M.D. Ediger, P. Harrowell and L. Yu: Crystal growth kinetics exhibit a fragility-dependent decoupling from viscosity. *Journal of Chemical Physics.* **128**(3), 034709 (2008).
- 37. C.A. Angell: Water-II is a strong liquid. J. Phys. Chem. 97(24), 6339 (1993).
- 38. S. Wei, P. Lucas and C.A. Angell: Phase change alloy viscosities down to T<sub>g</sub> using Adam-Gibbs-equation fittings to excess entropy data: A fragile-to-strong transition. *J. Appl. Phys.* **118**(3), 034903 (2015).

- 39. S.L. Lai, G. Ramanath, L.H. Allen, P. Infante and Z. Ma: High-speed (10<sup>4</sup>°C/s) scanning microcalorimetry with monolayer sensitivity (J/m²). *Appl. Phys. Lett.* **67**(9), 1229 (1995).
- 40. M.D. Grapes, T. LaGrange, L.H. Friedman, B.W. Reed, G.H. Campbell, T.P. Weihs and D.A. LaVan: Combining nanocalorimetry and dynamic transmission electron microscopy for in situ characterization of materials processes under rapid heating and cooling. *Review of Scientific Instruments.* **85**(8), 084902 (2014).
- 41. M.D. Grapes, M.K. Santala, G.H. Campbell, D.A. LaVan and T.P. Weihs: A detailed study of the Al<sub>3</sub>Ni formation reaction using nanocalorimetry. *Thermochimica Acta.* **658**, 72 (2017).
- 42. M.R. Armstrong, K. Boyden, N.D. Browning, G.H. Campbell, J.D. Colvin, W.J. DeHope, A.M. Frank, D.J. Gibson, F. Hartemann, J.S. Kim, W.E. King, T.B. LaGrange, B.J. Pyke, B.W. Reed, R.M. Shuttlesworth, B.C. Stuart and B.R. Torralva: Practical considerations for high spatial and temporal resolution dynamic transmission electron microscopy. *Ultramicroscopy.* **107**(4-5), 356 (2007).
- 43. T. LaGrange, B.W. Reed, M.K. Santala, J.T. McKeown, A. Kulovits, J.M.K. Wiezorek, L. Nikolova, F. Rosei, B.J. Siwick and G.H. Campbell: Approaches for ultrafast imaging of transient materials processes in the transmission electron microscope. *Micron.* 43(11), 1108 (2012).
- 44. G.H. Campbell, J.T. McKeown and M.K. Santala: Time resolved electron microscopy for in situ experiments. *Applied Physics Reviews.* **1**(4), 041101 (2014).
- 45. M.K. Santala, B.W. Reed, S. Raoux, T. Topuria, T. LaGrange and G.H. Campbell: Nanosecond-scale time-resolved electron imaging during laser crystallization of GeTe. *Physica Status Solidi B.* **249**(10), 1907 (2012).
- 46. M.K. Santala, B.W. Reed, S. Raoux, T. Topuria, T. LaGrange and G.H. Campbell: Irreversible reactions studied with nanosecond TEM movies: laser crystallization of phase change materials. *Appl. Phys. Lett.* **102**(17), 174105 (2013).
- 47. M.K. Santala, B.W. Reed, T. Topuria, S. Raoux, S. Meister, Y. Cui, T. LaGrange, G.H. Campbell and N.D. Browning: Nanosecond *in situ* transmission electron microscope studies of the reversible Ge<sub>2</sub>Sb<sub>2</sub>Te<sub>5</sub> crystalline ⇔ amorphous phase transformation. *J. Appl. Phys.* **111**(2), 024309 (2012).
- 48. J.C. Mauro, Y.Z. Yue, A.J. Ellison, P.K. Gupta and D.C. Allan: Viscosity of glass-forming liquids. *Proc. Natl. Acad. Sci. U. S. A.* **106**(47), 19780 (2009).
- 49. B.L. Zink and F. Hellman: Specific heat and thermal conductivity of low-stress amorphous Si-N membranes. *Solid State Communications*. **129**(3), 199 (2004).
- 50. F. Yi, L.H. Friedman, R. Chen and D.A. LaVan: Sample pattern and temperature distribution in nanocalorimetry measurements. *Journal of Thermal Analysis and Calorimetry*. **138**(5), 3367 (2019).
- 51. F. Yi, M.D. Grapes and D.A. LaVan: Practical Guide to the Design, Fabrication, and Calibration of NIST Nanocalorimeters. *Journal of Research of the National Institute of Standards and Technology.* **124**, 3367 (2019).
- 52. F. Tabatabaei, G. Boussinot, R. Spatschek, E.A. Brener and M. Apel: Phase field modeling of rapid crystallization in the phase-change material AIST. *J. Appl. Phys.* **122**(4), 045108 (2017).
- 53. T. Matsunaga, Y. Umetani and N. Yamada: Structural study of a Ag<sub>3.4</sub>In<sub>3.7</sub>Sb<sub>76.4</sub>Te<sub>16.5</sub> quadruple compound utilized for phase-change optical disks. *Phys. Rev. B.* **64**(18), 184116 (2001).
- 54. J. Akola and R.O. Jones: Structure of liquid phase change material AgInSbTe from density functional/molecular dynamics simulations. *Appl. Phys. Lett.* **94**(25), 3 (2009).
- 55. J.A. Kalb, F. Spaepen and M. Wuttig: Kinetics of crystal nucleation in undercooled droplets of Sb- and Te-based alloys used for phase change recording. *J. Appl. Phys.* **98**(5), 054910 (2005).

# **Figures**

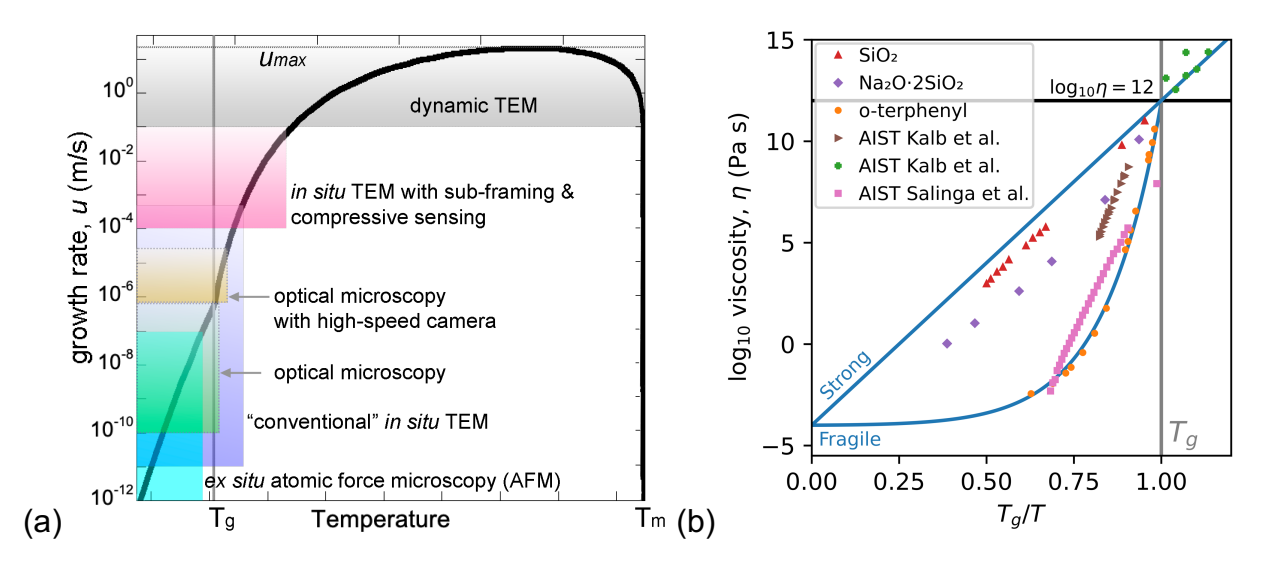


**FIG. 1** (a) Schematic of the isothermal crystal growth rate, u(T), for a generalized PCM. The kink at  $T_g$  is to highlight the change from a solid-solid to a liquid-solid growth mechanism. The region just above  $T_g$  is important due to its relationship with the liquid fragility. Crystallization around  $u_{max}$  is difficult to observe directly because it exceeds 1 m/s for most PCMs. Microscopic experimental methods  $^{10, 16-20}$  are mapped to ranges where they potentially have both adequate spatial and temporal resolution to image growing grains in a PCM during crystallization. (b) Angell plot of log  $\eta$  vs. inverse temperature normalized by  $T_g$  showing the viscosity as a function of the reduced glass transition for a strong glass (SiO<sub>2</sub>), a fragile glass (o-terphenyl), Na<sub>2</sub>O·2SiO<sub>2</sub>,  $^{35}$  and for AIST alloys,  $^{12,16-17, 56}$  adapted from figures in references [12, 35]. Data for AIST above  $T_g$  is calculated from growth rate measurements.  $^{16-17}$ 

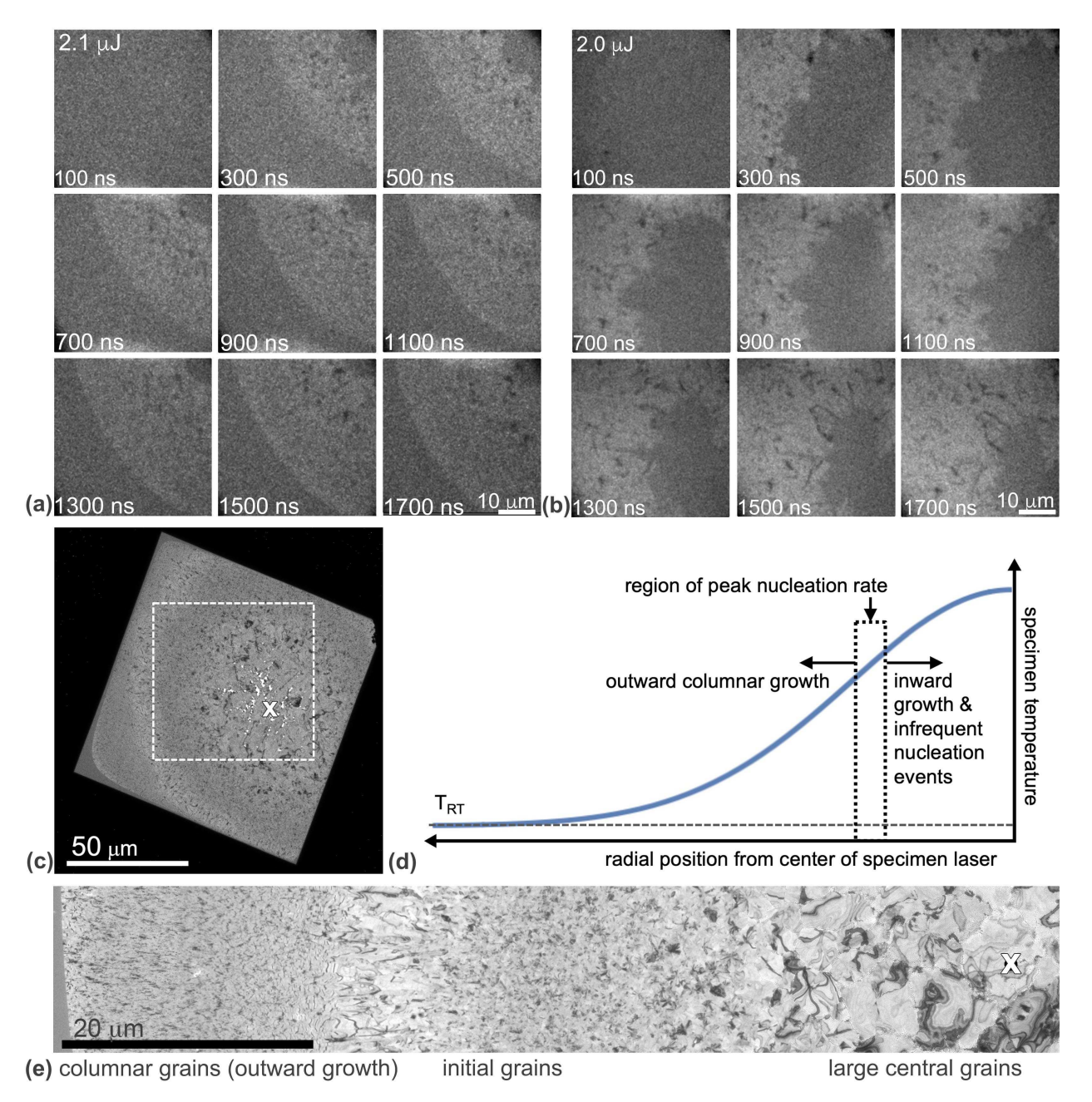


**FIG. 2** (a, b) Time-resolved DTEM imaging of laser-induced crystallization in as-deposited AIST. The time given in each frame is relative to the peak intensity of the 12-ns specimen laser pulse. For clarity, a median filter has been applied to the images in the figure to reduce shot noise. (c) The dashed box indicates the region imaged in (b) with the approximate center of the specimen laser pulse marked with an "x". (d) Schematic of the temperature profile induced by laser heating. (e) Detail of the microstructure after crystallization showing the grain morphology which changes with distance from the center of the laser pulse (marked with an "x").

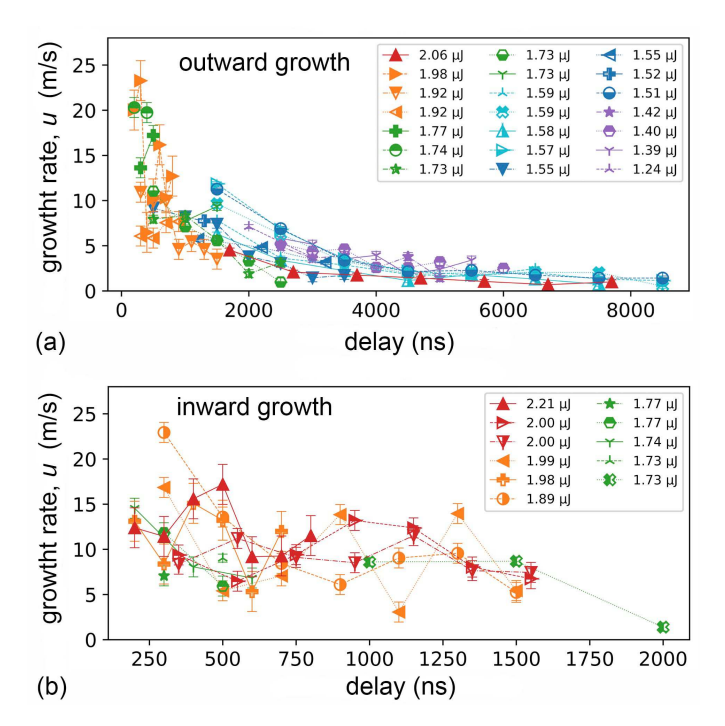
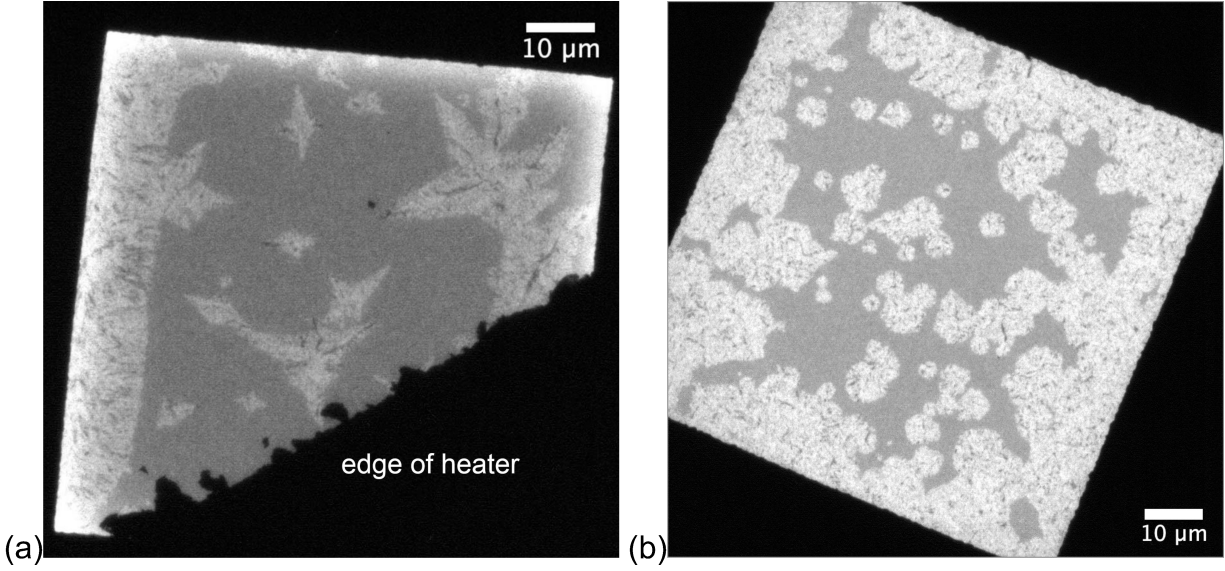
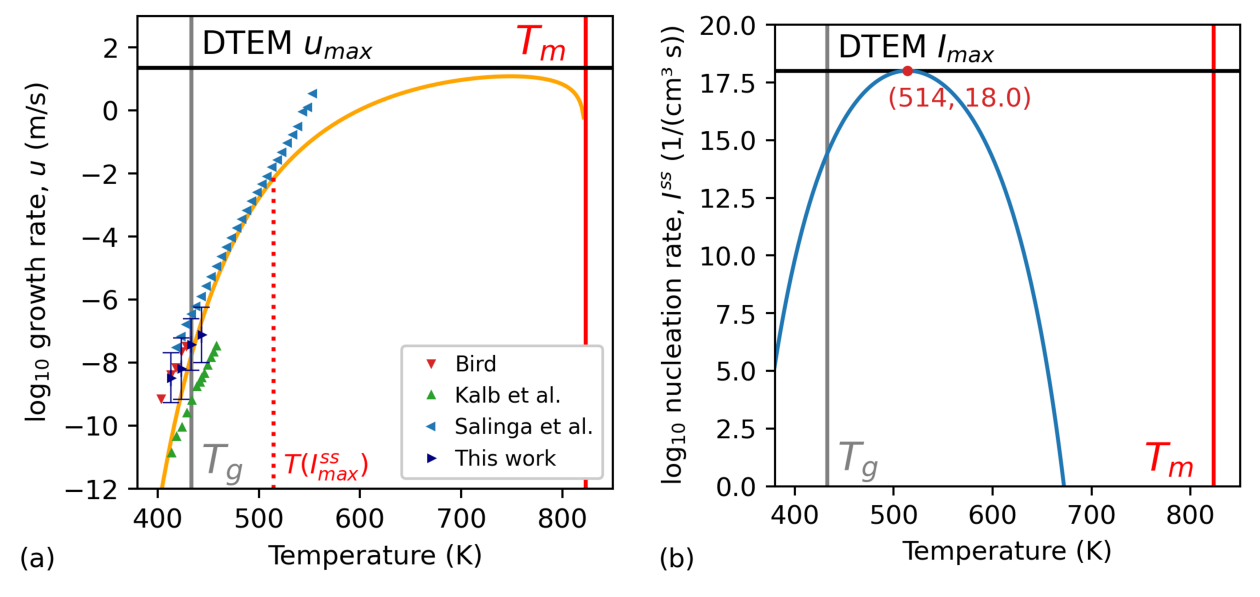


FIG. 3 High temperature growth rate versus the time passed since the specimen laser pulse from DTEM experiments for growth (a) outward and (b) inward from the initially formed crystalline annulus of grains. The values are calculated for each interval between sub-frames and the data are plotted at the time of the earlier sub-frame for each time interval. The first data point for each energy indicates the first frame with visible crystalline material. The error bars represent the error stemming from uncertainty in the manual determination of the position of the amorphous/crystalline interface.



**FIG. 4** Frames from a video capture at low magnification showing isothermal crystallization of AIST at (a) 433 K and (b) 413 K using a Gatan heating holder. The left edge of the window in (a) was precrystallized at T<sub>RT</sub> using the condensed electron beam. Crystalline grains (mottled light gray) nucleated within the amorphous (featureless dark gray) are star-shaped at 433 K and equiaxed at 413 K. The anisotropic growth in (a) appears related to the crystallographic direction of growth.



**FIG. 5** (a) Crystal growth rates and (b) nucleation rates for as-deposited Ag<sub>3</sub>In<sub>4</sub>Sb<sub>76</sub>Te<sub>17</sub> measured with DTEM and *in situ* TEM heating with a furnace-style heating holder plotted with growth rate data from this alloy from *in situ* optical microscopy (Bird<sup>17</sup>) and data from *ex situ* AFM (Kalb *et al.*<sup>16</sup>) and optical reflectivity (Salinga et al.<sup>15</sup>) for similar AIST alloys. DTEM experiments are used to determine  $u_{max}$  and estimate  $I_{max}$  (horizontal lines in (a) and (b), respectively). The fit models from EQN. [1] and [3] are plotted as the smooth curves with the parameters in Tables 1 and 2.

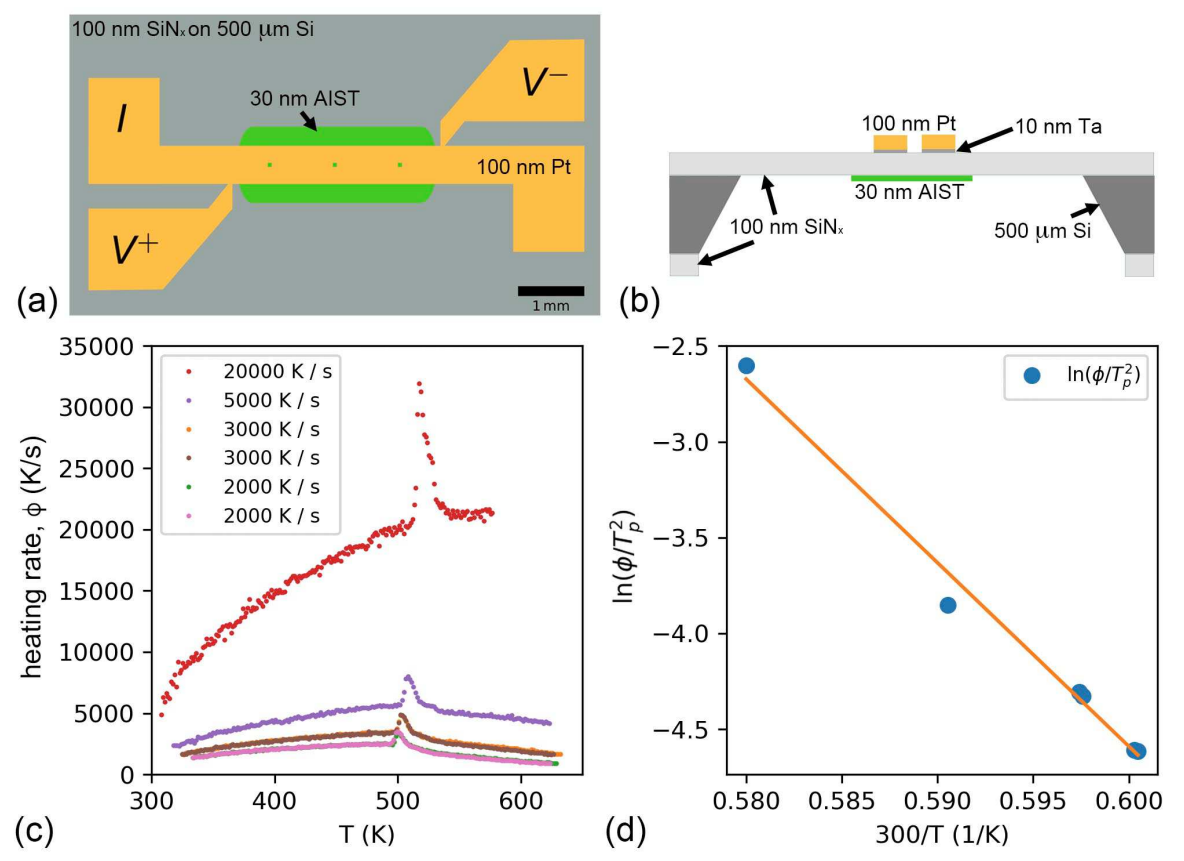


FIG. 6 Schematic of a nanocalorimeter with a deposited layer of AIST shown in (a) top view and (b) in cross section (not to scale) (c) preliminary calorimetric data, where the data from the two 2000 K/s and 3000 K/s ramps overlap almost completely (d) Kissinger plot derived from the data in (c).

# **Tables**

TABLE 1 Fixed parameters used in the models for isothermal nucleation and growth

Physical Property	Value	Stoichiometry	Source
melting temperature, $T_m$	823 K	$Ag_{3.4}In_{3.7}Sb_{76.4}Te_{16.5}$	Matsunaga et al. <sup>24</sup>
enthalpy of fusion, $\Delta h_f$	17.0 kJ/mol	$Ag_{4}In_{3}Sb_{67}Te_{26}$	Tabatabaei et al.52
density, $\rho$	$6.56 \text{ g/cm}^3$	$Ag_{3.4}In_{3.7}Sb_{76.4}Te_{16.5}$	Matsunaga et al.53
jump distance, $\lambda$	0.3 nm	$Ag_{3.5}In_{3.8}Sb_{75}Te_{17.7}$	Akola and Jones <sup>54</sup>
grain radius, $r$	1 μm		see text
molar mass, $M$ high temperature limit of viscosity $\eta_{\infty}$	122 g/mol 10 <sup>-3.31</sup> Pa s	$\begin{array}{l} Ag_{3}In_{4}Sb_{76}Te_{17} \\ Ag_{5.5}In_{6.5}Sb_{59}Te_{29} \end{array}$	Orava <i>et al</i> . <sup>32</sup>

**TABLE 2** Fitting parameters used in the models for isothermal nucleation and growth. Initial values are derived from literature sources as indicated.

Physical property	Initial value	Source	Fitted value	Error
interfacial energy, $\sigma$	$0.055\ J/m^2$	Kalb et al.55	$0.1 \text{ J/m}^2$	$0.02\ J/m^2$
kinetic fragility, m	135	Salinga <i>et al</i> . <sup>15</sup>	79	46
glass transition, T <sub>g</sub>	433 K	Kalb et al.26	398 K	24 K

**TABLE 3** Activation energy for crystallization,  $E_x$ , for AIST from preliminary nanocalorimetry compared to activation energies of crystal growth,  $E_{cg}$ , from isothermal experiments.

Method	$E_{x}$ (eV)	$E_{cg}\left( eV\right)$	Material	Source
nanocalorimetry	2.51		as-deposited Ag <sub>3</sub> In <sub>4</sub> Sb <sub>76</sub> Te <sub>17</sub>	This work
in situ optical microscopy		2.43	as-deposited Ag <sub>3</sub> In <sub>4</sub> Sb <sub>76</sub> Te <sub>17</sub>	Bird <sup>17</sup>
in situ laser reflectivity		2.7	melt-quenched Ag <sub>4</sub> In <sub>3</sub> Sb <sub>67</sub> Te <sub>26</sub>	Salinga <i>et al</i> . 15
ex situ AFM		2.9	as-deposited Ag <sub>5.5</sub> In <sub>6.5</sub> Sb <sub>59</sub> Te <sub>29</sub>	Kalb et al. 16